Materials Advances

ROYAL SOCIETY OF CHEMISTRY

COMMUNICATION

View Article Online
View Journal | View Issue

Cite this: *Mater. Adv.*, 2022, 3, 6157

Received 29th May 2022,
Accepted 4th July 2022

DOI: 10.1039/d2ma00606e

rsc.li/materials-advances

Iodine-induced electrical conductivity of novel columnar lanthanide metal–organic frameworks based on a butterfly-shaped π-extended tetrathiafulvalene ligand†

Monica A. Gordillo, Paola A. Benavides, Colin McMillen and Sourav Saha *

Novel columnar lanthanide metal–organic frameworks (Ln-MOFs) based on a butterfly-shaped electron-rich π-extended tetrathia-fulvalene ligand (ExTTFTB) were synthesized and their electronic properties were investigated. Upon iodine-induced ligand oxidation, the Tb-MOF displayed *ca.* 100-fold higher electrical conductivity (5×10^{-7} S m^{-1}) than the neutral pristine MOF.

Metal–organic frameworks (MOFs)[1] have emerged as one of the most attractive functional materials due to their diverse structures, properties, and functions,[2–11] which can be easily fine-tuned by introducing different organic ligands and metal ions. The introduction of redox-active ligands[12,13] and/or metal ions[14–18] endows MOFs with mobile charge-carriers and helps create charge transport pathways, rendering them electrically conducting[7,8] and expanding their utility in various energy production, transport, and storage systems, such as batteries, transistors, capacitors, photovoltaics and fuel cells, and so on.[7,8,19–21] Among various redox-active building blocks, electron-rich tetrathiafulvalene (TTF) ligands have been used extensively to construct electrically conducting MOFs[22–25] because (i) the TTF cores can be easily functionalized with different coordinating groups, such as carboxylic acids and pyridines, to enable MOF formation, (ii) they can be oxidized easily and reversibly to stable TTF$^{\bullet+}$ radical cations and TTF^{2+} dications to enhance the charge-carrier concentration of the corresponding MOFs,[26–45] and (iii) TTF ligands can form extended π-stacks that can facilitate long-range through-space charge transport within the MOFs.[38,39]

Aiming to construct new MOF architectures that would not only possess adequate charge-carrier concentration but also efficient charge transport pathways, recently, we introduced[40] a butterfly-shaped electron-rich π-extended tetrathiafulvalene ligand containing four benzoate groups (ExTTFTB) that can coordinate metal ions. The ExTTFTB ligand has a convex π-surface consisting of a boat-shaped anthracene core attached to two 1,3-dithiolene rings at the 9- and 10-positions, which create a dihedral angle of ∼81°. This unique shape of the ExTTFTB ligand led to the formation of a novel double-helical Zn-EXTTFTB MOF in which, the convex ExTTF cores formed extended π–π-interactions along the seams of the neighboring strands. Upon iodine-mediated partial oxidation of about half of the ExTTFTB ligands to ExTTFTB$^{\bullet+}$ radical cations in each double-helical strand, extended ExTTFTB/ExTTFTB$^{\bullet+}$ π-donor/acceptor chains were formed along the seams of adjacent strands, which facilitated long-range charge movement and engendered 10^4-fold higher electrical conductivity (∼10^{-4} S m^{-1}) than that of the pristine MOF. However, in the 2D double-helical Zn-EXTTFTB MOF, not all carboxylate arms of the ExTTFTB ligand were coordinated extensively with the Zn^{2+} ions, which prevented the formation a 3D architecture and led us to envision that if all carboxylate groups of the ExTTFTB coordinated extensively with the metal cluster nodes, then they could potentially form 3D MOFs. Based on this design principle, we have employed Ln^{3+} ions (Eu^{3+}, Tb^{3+}, and Er^{3+}), postulating that the larger ionic radii and higher coordination number of Ln^{3+} ions should allow more extensive coordination of multiple ExTTFTB ligands at the same time, which should lead to the formation of a novel 3D columnar MOF architecture defined by the curvature of convex ExTTFTB ligands. Herein, we report the synthesis, structural characterization, and electronic and optical properties of a new 3D columnar Ln-ExTTFTB MOF architecture, which displayed almost two orders of magnitude higher electrical conductivity (10^{-7} S m^{-1}) upon iodine-mediated oxidation of the ExTTFTB ligands to ExTTFTB$^{\bullet+}$ radical cations possibly due to increased charge-carrier concentration.

The solvothermal reaction between ExTTFTB and $Ln(NO_3)_3 \cdot 5H_2O$ (Ln^{3+} = Eu^{3+}, Tb^{3+}, and Er^{3+}) in a mixture of dimethylformamide (DMF), H_2O, and trifluoroacetic acid (TFA) at 65 °C yielded reddish orange crystals of the corresponding Ln-ExTTFTB MOFs (Fig. 1A, see ESI† for details). Single crystal X-ray diffraction (SXRD) analysis revealed that all three Ln-MOFs were isostructural and

Department of Chemistry, Clemson University, 211 S. Palmetto Blvd., Clemson, SC, 29634, USA. E-mail: souravs@clemson.edu

† Electronic supplementary information (ESI) available: Synthesis, characterization, and additional experimental data of Ln-MOFs, crystallographic data CCDC 2156276–2156278. For ESI and crystallographic data in CIF or other electronic format see DOI: https://doi.org/10.1039/d2ma00606e

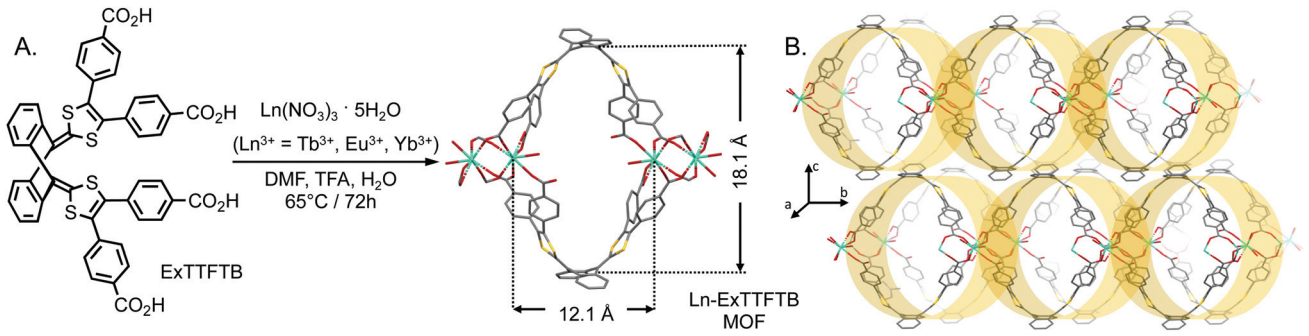

Fig. 1 (A) Synthetic scheme and (B) single crystal X-ray (SXRD) structure of Ex-TTFTB-based Ln-MOFs (C, gray; O, red; S, yellow; and Ln, cyan; H-atoms and solvent molecules are omitted for clarity).

possessed a 3D columnar architecture (Fig. 1B) with a triclinic $P\bar{1}$ space group. The asymmetric unit of representative Tb-MOF featured one Tb^{3+} ion, one ExTTFTB ligand, one Tb-coordinated H_2O, and one free DMF molecule. In contrast to our previously reported 2D double-helical Zn-ExTTFTB MOF[40] that contained two distinct Zn-nodes because only three carboxylate groups of each ExTTFTB were involved in Zn-coordination, in 3D Ln-ExTTFTB MOFs, all Ln^{3+} ions have the same coordination environment, and all four carboxylate groups of each ligand are coordinated to Ln^{3+} ions. For example, in Tb-MOF, the four carboxylate groups of each ExTTFTB ligand are coordinated to six Tb^{3+} ions: two *trans*-carboxylate groups coordinated four Tb^{3+} ions in a bridging bidentate mode with each binding two Tb^{3+} ions, the third carboxylate group chelated a Tb^{3+} ion in a bidentate mode, and the fourth one coordinated a Tb^{3+} ion in a monodentate fashion and remained in the acid form. The octa-coordinated Tb^{3+} ions of this MOF are coordinated by six carboxylate groups—four in a bridging bidentate mode, one in a chelating bidentate mode, and another in a monodentate mode—and one water molecule (Fig. S1, ESI†). The Ln–O bond lengths—2.352(4)–2.500(5) Å for Eu-MOF, 2.296(7)–2.507(4) Å for Tb-MOF, and 2.236(8)–2.462(4) Å for Er-MOF—roughly followed the ionic radius trend.[30,43] The face-to-face oriented convex ExTTFTB ligands connected by Ln-cluster nodes formed large ovoid channels (*ca.* 18 × 12 Å in diameter) extended along the crystallographic *a*-axis and the Ln-nodes connected the parallel columns along the *b*-axis forming the 3D columnar arrays, which were packed along the *c*-axis (Fig. 1B). The Ln-coordination further augmented the curvature of the convex ExTTFTB ligands, which formed the walls of these columns. In Ln-MOFs, the dihedral angles between the two 1,3-dithiolene rings of the ExTTFTB ligand were 65–67° (*vs.* 81° in the free ligand). The columnar arrays of Ln-MOFs are packed in a similar fashion as double-helical strands of Zn-ExTTFTB MOF,[40] *i.e.*, the convex ExTTFTB ligands of a given array of coordinatively linked columns protruded into the grooves of adjacent arrays (Fig. 1B). However, unlike the double-helical Zn-ExTTFTB MOF, in the Ln-EXTTFTB MOFs, the 1,3-dithiolene rings of the ExTTFTB ligands of neighboring columnar arrays were not aligned co-facially, which prevented meaningful intermolecular π–π stacking interactions (Fig. S2, ESI†) and efficient through-space charge movement (*vide infra*). The C=C bond lengths between the central anthracene and 1,3-dithiolene rings are *ca.* 1.34–1.35 Å, which is consistent with a double-bond character, indicating that the ExTTFTB ligands in Ln-MOFs are mostly neutral.[40,41] Since all three Ln-ExTTFTB MOFs are isostructural, herein, we used the representative Tb-ExTTFTB MOF for further studies of electronic and optical properties, which, in principle, can be extrapolated to all three MOFs.

The experimental and simulated powder X-ray diffraction (PXRD) patterns of pristine Tb-MOF are in good agreement (Fig. S3, ESI†). The higher intensity of some peaks in the experimental PXRD profile and some discrepancies between experimental and simulated patterns could be attributed to the preferred orientation of MOF crystallites (extensive grinding of MOF powders to disrupt such orientation diminished crystallinity).

To oxidize the electron-rich ExTTFTB ligands of the Tb-MOF, we exposed it to I_2 vapor.[40] After I_2-treatment, the orange Tb-MOF turned into a brown powder, which was washed thoroughly to remove any physisorbed I_2. The PXRD pattern of the I_2-treated Tb-MOF was in good agreement with that of the pristine material (Fig. S3, ESI†), suggesting that it remained mostly crystalline after I_2-induced partial oxidation of the ExTTFTB ligands to $ExTTFTB^{\bullet+}$ radical cations (*vide infra*) although some signals became slightly broader and weaker, which is not uncommon in other I_2-treated TTF-based MOFs.[40] Thermogravimetric analysis revealed that both pristine and I_2-treated Tb-MOFs (Fig. S4, ESI†) lost *ca.* 9% weight before 150 °C, which corresponded to the loss of residual solvent, followed by a plateau until *ca.* 320 °C, suggesting that no physisorbed I_2 was left in the latter.

The I_2-mediated oxidation of the Tb-ExTTFTB MOF was confirmed by quantitative electron paramagnetic resonance (EPR) spectroscopy (Fig. 2).[38,39] Whereas the pristine Tb-MOF displayed a small EPR signal indicating the presence of a small fraction of aerobically oxidized paramagnetic $ExTTFTB^{\bullet+}$ radical cations (1.7×10^{19} spins mol^{-1}), the I_2-treated Tb-MOF showed a significantly stronger EPR signal, revealing that I_2 produced a much greater population of $ExTTFTB^{\bullet+}$ radical cations (7.7×10^{20} spins mol^{-1}). Thus, the latter contained a significantly higher charge carrier concentration, which led to enhanced framework conductivity.

The diffuse reflectance spectrum (DRS) of the pristine Tb-MOF displayed (Fig. 3A) an absorption band with an onset at 618 nm, which corresponded to an optical band gap

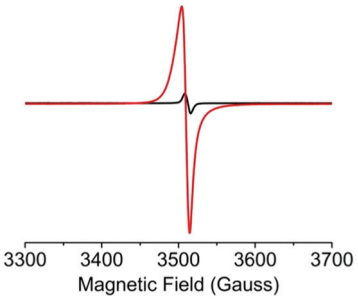

Fig. 2 Solid-state EPR spectra of the pristine (black) and iodine-treated (red) Tb-MOF show I_2-induced oxidation of ExTTFTB ligands to paramagnetic ExTTFTB$^{\bullet+}$ radical cations.

of *ca.* 2 eV. In contrast, the I_2-treated Tb-MOF displayed a broader absorption band through *ca.* 760 nm, which corresponded to a narrower optical band gap of 1.6 eV.[40] These optical band gaps of the pristine and I_2-treated Tb-MOFs are in good agreement with those calculated from their respective Tauc plots (2.1 and 1.7 eV) (Fig. 3B). The narrower band gap of the latter is attributed to I_2-mediated oxidation of the ExTTFTB to an ExTTFTB$^{\bullet+}$ radical cation, which absorbs at a longer wavelength.

Finally, to determine the effects of the I_2-induced oxidation of the ExTTFTB ligands of Tb-MOF on its electrical conductivity, we measured the current–voltage (*I–V*) relationships (Fig. 4) of pressed pellets of the pristine and I_2-treated Tb-MOF by the two-probe method using pellets placed between two stainless steel electrodes surrounded by a snug-fit Teflon tube.[38–40] Both materials displayed linear *I–V* plots, albeit with different slopes, indicating ohmic conduction. The electrical conductivity of the I_2-treated Tb-MOF (5×10^{-7} S m^{-1}) was two orders of magnitude higher than that of the pristine material (7×10^{-9} S m^{-1}), which can be attributed to its enhanced charge carrier concentration provided by a large ExTTFTB$^{\bullet+}$ population. However, the conductivity of the I_2-treated columnar Tb-MOF was lower than that of the previously reported I_2-treated double-helical Zn-ExTTFTB MOF ($\sim 10^{-4}$ S m^{-1}).[40] This difference can be attributed to the lack of π-donor/acceptor interactions between the spatially separated ExTTFTB ligands of the I_2-treated columnar Tb-MOF, which hindered through-space charge movement, whereas the extended ExTTFTB/ExTTFTB$^{\bullet+}$ π-donor/acceptor chains located along the seams of adjacent double helical

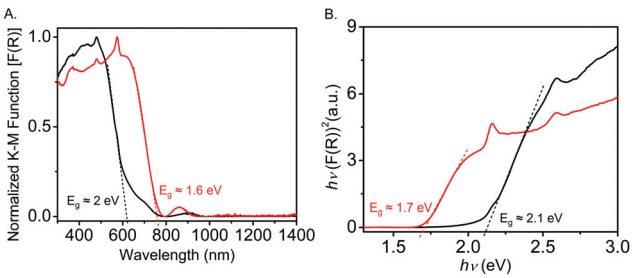

Fig. 3 (A) Diffusion reflectance spectra and (B) Tauc plots of the pristine (black) and iodine-treated (red) Tb-MOF.

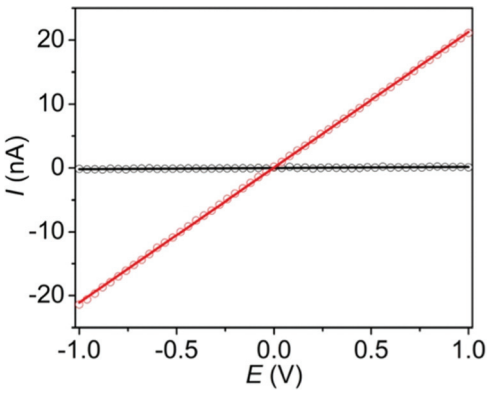

Fig. 4 The *I–V* plots of pristine (black) and iodine-treated (red) Tb-MOF pellets show higher conductivity of the latter.

strands of the I_2-treated Zn-ExTTFTB MOF facilitated long-range charge movement. As often found in other electrically conducting Ln-MOFs,[28,29,43–45] the ionic Tb–O bonds cannot support through-bond charge movement, leaving less efficient redox-hopping as the predominant charge transport mechanism in the Tb-ExTTFTB MOF. Due to grain-boundary and contact resistances, bulk conductivities measured with MOF pellets consisting of microcrystallites are usually 2–3 orders of magnitude smaller than the corresponding single crystal conductivity[7,8,46] (in rare events suitable crystals are available for such measurements).

In summary, we have synthesized new isostructural 3D columnar Ln-MOFs based on a butterfly-shaped electron-rich ExTTFTB ligand. While ExTTFTB formed a 2D double helical MOF with Zn^{2+}, the introduction of larger Ln^{3+} ions with higher coordination number led to the formation of 3D columnar MOFs containing coordinatively linked parallel columns made of face-to-face oriented convex ExTTFTB ligands. I_2-mediated oxidation of the Tb-MOF enhanced its electrical conductivity from *ca.* 10^{-9} to 10^{-7} S m^{-1} due to the formation of EXTTFTB$^{\bullet+}$ radical cations, which increased the charge-carrier concentration, although the MOF lacked well-defined through-bond or through-space charge-transport pathways. Thus, these studies yielded novel 3D columnar Ln-MOFs and demonstrated that while improved charge-carrier concentration can modestly enhance the electrical conductivity of redox-active MOFs, efficient charge movement is vital for attaining very high electrical conductivity.

We acknowledge the US National Science Foundation (award no. NSF-1809092) for financial support for this work.

Conflicts of interest

There are no conflicts to declare.

References

1 H. Furukawa, K. E. Cordova, M. O'Keeffe and O. M. Yaghi, *Science*, 2013, **341**, 1230444-1–12.

2 J.-R. Li, J. Sculley and H.-C. Zhou, *Chem. Rev.*, 2012, **112**, 869–932.
3 K. Sumida, D. L. Rogow, J. A. Mason, T. M. McDonald, E. D. Bloch, Z. R. Herm, T. Bae and J. R. Long, *Chem. Rev.*, 2012, **112**, 724–781.
4 P. Horcajada, R. Gref, T. Baati, P. K. Allan, G. Maurin, P. Couvreur, G. Férey, R. E. Morris and C. Serre, *Chem. Rev.*, 2012, **112**, 1232–1268.
5 V. Stavila, A. A. Talin and M. D. Allendorf, *Chem. Soc. Rev.*, 2014, **43**, 5994–6010.
6 L. Sun, M. G. Campbell and M. Dincă, *Angew. Chem., Int. Ed.*, 2016, **55**, 3566–3579.
7 L. S. Xie, G. Skorupskii and M. Dincă, *Chem. Rev.*, 2020, **120**, 8536–8580.
8 H. Wang, Q.-L. Zhu, R. Zou and Q. Xu, *Chemistry*, 2017, **2**, 52–80.
9 M. A. Gordillo, D. K. Panda and S. Saha, *ACS Appl. Mater. Interfaces*, 2019, **11**, 3196–3206.
10 T. Zhang and W. Lin, *Chem. Soc. Rev.*, 2014, **43**, 5982–5993.
11 E. A. Dolgopolova and N. B. Shustova, *MRS Bull.*, 2016, **41**, 890–896.
12 B. Ding, M. B. Solomon, C. F. Leong and D. M. D'Alessandro, *Coord. Chem. Rev.*, 2021, **439**, 213891.
13 D. M. D'Alessandro, *Chem. Commun.*, 2016, **52**, 8957–8971.
14 D. Sheberla, L. Sun, M. A. Blood-Forsythe, S. Er, C. R. Wade, C. K. Brozek, A. Aspuru-Guzik and M. Dincă, *J. Am. Chem. Soc.*, 2014, **136**, 8859–8862.
15 J.-H. Dou, L. Sun, Y. Ge, W. Li, C. H. Hendon, J. Li, S. Gul, J. Yano, E. A. Stach and M. Dincă, *J. Am. Chem. Soc.*, 2017, **139**, 13608–13611.
16 J. Clough, N. M. Orchanian, J. M. Skelton, A. J. Neer, S. A. Howard, C. A. Downes, L. F. J. Piper, A. Walsh, B. C. Melot and S. C. Marinescu, *J. Am. Chem. Soc.*, 2019, **141**, 16323–16330.
17 G. Chen, L. B. Gee, W. Xu, Y. Zhu, J. S. Lezama-Pacheco, Z. Huang, Z. Li, J. T. Babicz, S. Choudhury, T. H. Chang, E. Reed, E. I. Solomon and Z. Bao, *J. Am. Chem. Soc.*, 2020, **142**, 21243–21248.
18 L. S. Xie, L. Sun, R. Wan, S. S. Park, J. A. Degayner, C. H. Hendon and M. Dincă, *J. Am. Chem. Soc.*, 2018, **140**, 7411–7414.
19 W.-H. Li, K. Ding, H.-R. Tian, M.-S. Yao, B. Nath, W.-H. Deng, Y. Wang and G. Xu, *Adv. Funct. Mater.*, 2017, **27**, 1702067.
20 D. Sheberla, J. C. Bachman, J. S. Elias, C. J. Sun, Y. Shao-Horn and M. Dincă, *Nat. Mater.*, 2016, **16**, 220–224.
21 L. Wang, Y. Han, X. Feng, J. Zhou, P. Qi and B. Wang, *Coord. Chem. Rev.*, 2016, **307**, 361–381.
22 J. L. Segura and N. Martin, *Angew. Chem., Int. Ed.*, 2001, **40**, 1372–1409.
23 D. Canevet, M. Sallé, G. Zhang, D. Zhang and D. Zhu, *Chem. Commun.*, 2009, 2245–2269.
24 J. Liu, W. Zhou, J. Liu, I. Howard, G. Kilibarda, S. Schlabach, D. Coupry, M. Addicoat, S. Yoneda, Y. Tsutsui, T. Sakurai, S. Seki, Z. Wang, P. Lindemann, E. Redel, T. Heine and C. Wöll, *Angew. Chem., Int. Ed.*, 2015, **54**, 7441–7445.
25 H. Y. Wang, L. Cui, J. Z. Xie, C. F. Leong, D. M. D'Alessandro and J. L. Zuo, *Coord. Chem. Rev.*, 2017, **345**, 342–361.
26 T. C. Narayan, T. Miyakai, S. Seki and M. Dincă, *J. Am. Chem. Soc.*, 2012, **134**, 12932–12935.
27 H.-Y. Wang, J.-Y. Ge, C. Hua, C.-Q. Jiao, Y. Wu, C. F. Leong, D. M. D'Alessandro, T. Liu and J.-L. Zuo, *Angew. Chem., Int. Ed.*, 2017, **56**, 5465–5470.
28 L. S. Xie, E. V. Alexandrov, G. Skorupskii, D. M. Proserpio and M. Dincă, *Chem. Sci.*, 2019, **10**, 8558–8565.
29 J. Su, S. Yuan, J. Li, H. Y. Wang, J. Y. Ge, H. F. Drake, C. F. Leong, F. Yu, D. M. D'Alessandro, M. Kurmoo, J. L. Zuo and H. C. Zhou, *Chem. – Eur. J.*, 2021, **27**, 622–627.
30 F. Leong, C.-H. Wang, C. D. Ling and D. M. D'Alessandro, *Polyhedron*, 2018, **154**, 334–342.
31 S. S. Park, E. R. Hontz, L. Sun, C. H. Hendon, A. Walsh, T. Van Voorhis and M. Dincă, *J. Am. Chem. Soc.*, 2015, **137**, 1774–1777.
32 J. Su, S. Yuan, H.-Y. Wang, L. Huang, J.-Y. Ge, E. Joseph, J. Qin, T. Cagin, J.-L. Zuo and H.-C. Zhou, *Nat. Commun.*, 2017, **8**, 2008.
33 H. Y. Wang, Y. Wu, C. F. Leong, D. M. D'Alessandro and J. L. Zuo, *Inorg. Chem.*, 2015, **54**, 10766–10775.
34 H. Y. Wang, J. Su, J. P. Ma, F. Yu, C. F. Leong, D. M. D'Alessandro, M. Kurmoo and J. L. Zuo, *Inorg. Chem.*, 2019, **58**, 8657–8664.
35 Y. G. Weng, W. Y. Yin, M. Jiang, J. Le Hou, J. Shao, Q. Y. Zhu and J. Dai, *ACS Appl. Mater. Interfaces*, 2020, **12**, 52615–52623.
36 Z. N. Yin, Y. H. Li, Y. G. Sun, T. Chen, J. Xu, Q. Y. Zhu and J. Dai, *Inorg. Chem.*, 2016, **55**, 9154–9157.
37 D. Bechu, L. S. Xie, N. Le Breton, S. Choua, M. Dincă, M. W. Hosseini and S. A. Baudron, *Chem. Commun.*, 2020, **56**, 2407–2410.
38 S. Zhang, D. K. Panda, A. Yadav, W. Zhou and S. Saha, *Chem. Sci.*, 2021, **12**, 13379–13391.
39 M. A. Gordillo, P. A. Benavides, K. Spalding and S. Saha, *Front. Chem.*, 2021, **9**, 792.
40 M. A. Gordillo, P. A. Benavides, D. K. Panda and S. Saha, *ACS Appl. Mater. Interfaces*, 2020, **12**, 12955–12961.
41 J. Su, N. Xu, R. Murase, Z.-M. Yang, D. M. D'Alessandro, J.-L. Zuo and J. Zhu, *Angew. Chem., Int. Ed.*, 2021, **60**, 4789.
42 F. Gao, F. F. Zhu, X. Y. Wang, Y. Xu, X. P. Wang and J. L. Zuo, *Inorg. Chem.*, 2014, **53**, 5321–5327.
43 J. Su, T.-H. Hu, R. Murase, H.-Y. Wang, D. M. D'Alessandro, M. Kurmoo and J.-L. Zuo, *Inorg. Chem.*, 2019, **58**, 3698–3706.
44 J.-J. Hu, Y.-G. Li, H.-R. Wen, S.-J. Liu, Y. Peng and C.-M. Liu, *Dalton Trans.*, 2021, **50**, 14714–14723.
45 G. Skorupskii, B. A. Trump, T. W. Kasel, C. M. Brown, C. H. Hendon and M. Dincă, *Nat. Chem.*, 2020, **12**, 131–136.
46 L. Sun, S. S. Park, D. Sheberla and M. Dincă, *J. Am. Chem. Soc.*, 2016, **138**, 14772–14782.